TIP-VORTEX INVESTIGATION ON A ROTATING AND PITCHING ROTOR BLADE

Andreas Goerttler, Johannes N. Braukmann, Till Schwermer, Anthony D. Gardner and Markus Raffel
German Aerospace Center (DLR), Institute of Aerodynamics and Flow Technology,
Bunsenstraße 10, 37073, Göttingen, Germany
andreas.goerttler@dlr.de

ABSTRACT

The blade-tip vortex of a rotating and pitching DSA-9A blade was investigated numerically and experimentally. Numerical computations were performed using DLR's finite volume solver TAU and experimental data was gathered by using particle image velocimetry (PIV) carried out in a stereoscopic setup at the rotor test facility in Göttingen (RTG). Algorithms deriving the vortex position, swirl velocity, circulation and core radius were implemented. The agreement is better the lower the wake age, with numerical dissipation enlarging the blade-tip vortex in an artificial manner with increasing wake age. Nevertheless, the numerical simulations are able to predict swirl velocity and circulation well and help understanding the growth and development of the blade-tip vortices. A comparison with a nonrotating version of this blade showed that the circulation of the nonrotating blade was in the same order.

NOMENCLATURE

a, b	Major and minor axis of an ellipse
c	Blade chord length ($c = 0.072\,\mathrm{m}$)
c_t	Local thrust coefficient
C_T	Blade thrust coefficient ($C_T = F_z/(\rho_\infty(\Omega R)^2\pi R^2)$)
c_m	Local pitching moment coefficient
i	Inclination of an ellipse
M	Mach number
n	Vatistas swirl shape parameter
Q	$\Gamma_{0.2c}/C_l M^2 \cdot C_l M^2(\Theta_{\min})/\Gamma_{0.2c}(\Theta_{\min})$
r	Radial distance
R	Rotor blade radius ($R = 0.65\,\mathrm{m}$)
Re	Reynolds number based on chord
r_v	Vortex coordinates in radial direction (m)
ϕ_v	Vortex coordinates in azimuthal direction (°)
ρ_∞	Free stream flow density (kg/m^3)
t	Time (s)
T	Period time (s)
u_p	Axial velocity along x_p (m/s)
U	Velocity (m/s)
v_r	Radial velocity (m/s) ($v_r \hat{=} \dot{r}_v$)
v_ϕ	Swirl Velocity (m/s) ($v_\phi \hat{=} \dot{\phi}_v$)
v_Ψ	Inplane Velocity (m/s) ($v_\Psi = \sqrt{v_r^2 + v_\phi^2}$)
x	Curved distance between measurement position and blade tip trailing edge (m)
x_p, y_p, z_p	PIV plane coordinates in axial, outboard and downward direction (m)
y^+	Dimensionless wall distance
Δs	Edge length of cells in tip region
Γ	Circulation (m^2/s)
Θ	Blade pitch angle (°)
Ψ	Azimuth angle (°)
Ψ_V	Vortex age (°)
ω	Vorticity ($1/s$)
Ω	Rotational speed (23.6 Hz)
$\uparrow$	During upstroke motion
$\downarrow$	During downstroke motion

Subscripts

70	Condition at radial distance $r/R = 0.70$
77	Condition at radial distance $r/R = 0.77$
core	Edge of vortex core
root	Condition at the root of the blade
TTE	Blade tip trailing edge
tip	Condition at the tip of the blade
∞	Farfield condition

1. INTRODUCTION

Blade-tip vortices are still a challenging flow phenomenon in helicopter aerodynamics, since they induce drag and therefore influence the performance of the rotor. Blade-tip vortices arise due to pressure differences between the lower and upper surfaces driving the flow around the tip from the pressure side to the suction side. Depending on the shape of the tip several vortices can arise. Unlike fixed

wing aircraft, helicopters produce vortices which can be reingested by the rotor, striking the other blades leading to blade-vortex interaction. These interactions lead to a limitation of the flight envelope of the helicopter due to dynamic stall on the highly loaded rotor (see Richez [1]). Additionally, all interactions between vortices and structures result in a generation of impulsive aeroacoustic noise, which is relevant for the noise impact of a helicopter on areas surrounding flight paths and landing areas, as well as social acceptance of helicopter operations. Therefore, the understanding of the development and growth of blade-tip vortices is of great interest.

Early experimental work in the near field of a trailing vortex has been carried out by Chow et al. [2], who used a pressure probe to investigate the wing-tip vortex. The data of the rollup of the wing-tip vortex by Chow et al. [2] is still widely used by other researchers. The static measurements were conducted up to $x/c = 0.678$ downstream of the trailing edge showing a jet-like behavior of the vortex as the core axial velocity reached values 1.77 times the velocity outside the vortex. Devenport et al. [3], examined the structure and development of the wing-tip vortex with a hot wire probe, reporting that meandering of the vortex increased linearly with distance. Birch et al. [4] measured vortex properties of several different profiles with a pressure probe, observing an almost complete roll up after one chord length downstream. Martin et al. [5] used laser Doppler velocimetry (LDV) and particle image velocimetry (PIV) to evaluate the evolution of the tip vortex of a hovering rotor whereas McAlister [6] investigated the situation during a light climb detecting a square-root function for the rate of growth of the blade-tip vortex. A thoroughly numerical and experimental study was performed by Duraisamy et al. [7] who examined the on-blade formation of the tip vortex of a single bladed hovering rotor at $Re_{\text{tip}} = 272\,000$. They identified multiple vortex structures merging into a single coherent vortex in simulations and experiments.

Early comparisons between numerical and experimental results were carried out by Dacles-Mariani et al. [8], who compared their results with the experiment of Chow et al. [2] stating numerical guidelines resulting in good agreement with the experiment. Mohamed et al. [9] employed detached-eddy simulations (DES) on a pitching airfoil. They investigated the wing tip vortex at dynamic stall conditions reporting DES outperforming the Reynolds-averaged Navier-Stokes (RANS) equations. Recently Lombard et al. [10] validated their large-eddy simulations of the NACA 0012 profile with Chow et al. [2] results. They matched both the jetting velocity and the vortex spanwise location well. Garmann & Visbal [11–13] performed extensive numerical simulations of the NACA0012 profile at fixed and various oscillating conditions. They examined the vortex up to three chord lengths downstream observing an orbital motion. Furthermore, they found out that the vortex appearance (wake- or jet-like) is not driven by wake interactions. Most recently Lietzau et al. [14] compared numerical simulations with dual-plane PIV measurements of a single bladed hovering rotor. They reported difficulties in finding a grid-independent solution. The core radii of vortices at a young wake age ($\Psi_V < 15^\circ$) were consistently overpredicted by all investigated grids, grid stencils and turbulent models. The peak swirl velocity showed a better agreement with the PIV measurements leading to good agreement of the circulation of the vortex.

Recent experimental work of Wolf et al. [15] analyzed the wing-tip vortex of a pitching finite wing, with the DSA-9A airfoil and SPP8 blade tip noting that the tip vortex continued becoming stronger with increasing angle of attack even after the flow on the wing stalled. The corresponding numerical investigation has been carried out by Kaufmann et al. [16]. Both studies provided experimental and numerical data of circulation as well as swirl velocity without any rotary effects. Other investigations of the same nonrotating wing with the focus on dynamic stall has been carried out by Merz et al. [17] and Kaufmann et al. [18]. Schwermer et al. [19] analyzed experimentally dynamic stall at the rotor test facility (RTG) at the DLR in Göttingen [20]. The RTG rotor has been computed using stiff blades with prescribed motion in a simple farfield boundary condition by Letzgus et al. [21], resulting in good agreement with the experiment performed by Schwermer et al. [19].

This paper analyzes the blade-tip vortex of a rotor with high cyclic pitch. The rotor blades use also the DSA-9A airfoil and SPP8 blade tip and are thus a rotating version of Merz et al.'s [17] nonrotating finite wing. Both numerical predictions and experimental results are used in a combined manner to further investigate the tip vortex characteristics. For comparison with numerical data PIV was used to measure all three velocity components in a whole plane.

2. EXPERIMENTAL SETUP

The experimental investigations used the RTG, a facility in which a rotor with axial inflow ("Climb") is operated with high cyclic pitch. This generates a highly unsteady and three-dimensional flow which is periodic over one rotation. The pitch variation is analogous to that for helicopters in forward flight, but without the Mach and Reynolds number variation typical of that flight condition.

The RTG (see Fig. 1) consists of a rotor (1) with a horizontal axis, fed by a wind tunnel (2). The radius of the two bladed rotor is $R = 0.65\,\text{m}$ and the chord length of the blade is $c = 0.072\,\text{m}$. The blades use the 9% thick industry relevant helicopter profile DSA-9A, negatively and linearly twisted with $\Theta_{\text{root}} - \Theta_{\text{tip}} = 9.3^\circ$ between the incidence angle of the root ($r/R = 0.25$) and the tip. Similar to real helicopter configurations the blade tips are parabolically shaped, reducing the chord length at the blade tip to $c_{\text{tip}} = 0.024\,\text{m}$. One of the two rotor blades is instrumented with pressure sensors, four sensors at $r/R = 0.53$ and nine sensors at $r/R = 0.77$. Parameters of the experiment, which were also used for the simulations are listed in Tab. 1.

Low-speed PIV was performed on the wake of the airfoil

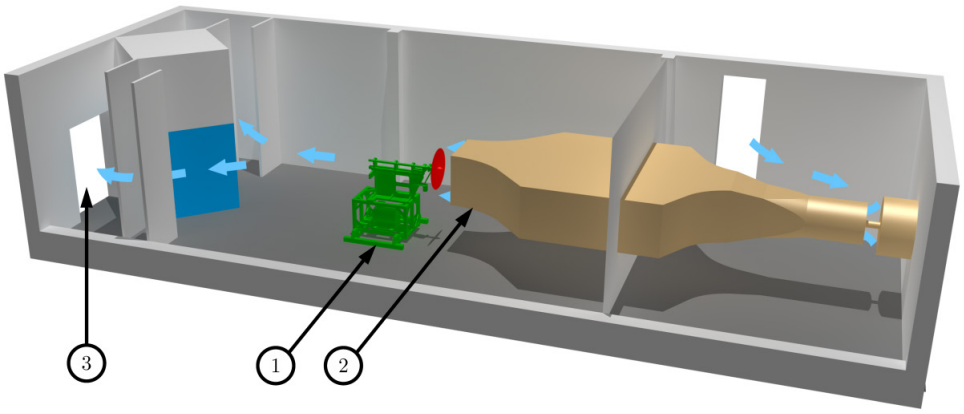

Figure 1: The rotor test facility (RTG) at the DLR in Göttingen (adapted from Schwermer et al. [20]).

Table 1: Parameters of experiment and simulation.

Parameter	Values
Chord, c	0.072 m
Radius, R	0.65 m
Airfoil	DSA-9A
Tip Mach-number, M_{tip}	0.28
Tip Reynolds-number, Re_{tip}	470000
Tip speed, U_{tip}	96.4 m/s
Θ_{root}	$23.0° - 6° \cdot \cos(2\pi \cdot t/T)$
Ω	23.6 Hz

using a stereoscopic setup. Figure 2 shows the investigated PIV planes which are marked with the wake age referenced to the $c/4$ line ($\Psi = 0°$). This nonintrusive technique records pictures of uniformly seeded flow. Two cameras in a stereoscopic setup took images, thus all three velocity components could be extracted. Schwermer et al. [19] give detailed information on the RTG and show experimental results. The PIV results have been analyzed and published by Braukmann et al. [22].

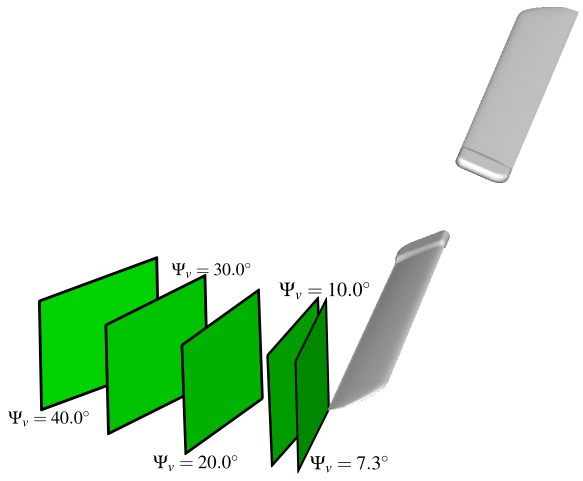

Figure 2: PIV planes at the RTG at the DLR in Göttingen.

3. NUMERICAL PROCEDURES

The numerical simulations are performed using the DLR-TAU [23] code. The Reynolds-averaged equations are closed by the Menter shear-stress transport (SST) turbulence model [24]. The TAU code is a node-based finite-volume solver and can be used with structured and unstructured grids. The hybrid unstructured grid was generated using CENTAUR$^{\text{TM}}$ and consists of three grid blocks connected by the grid overset method. The computations are second order in space and time, the inviscid fluxes were solved by a central method. The numerical setup corresponds to a simplified experimental setup. The two rotor blades are modeled as stiff blades, and a far-field free-stream condition is implemented in a spherical computational domain with a radius of 900 blade spans. Both blades consist of the same surface and structured boundary layer grid. The surface grid is refined in the tip area up to $\Delta s/c = 0.0034$. The hybrid grid consists of 30 prisms in the direction normal to the surface. The first cell height is set to $y_+ \sim \mathcal{O}(1)$ and a stretching factor of 1.2 is used to resolve the boundary layer. The area behind the trailing edge at the tip of one blade was further refined to resolve the tip vortex. Since structured cells have less dissipation a hexahedral block (see Fig. 3a) fitted to the tip path was constructed as Braun et al. [25] did for their investigations. The edge lengths of the hexahedrons are $\Delta s/c = 0.0034$ leading to 7.2 million hexahedral cells only in the small structured block. Due to high computational effort this fine resolution was only maintained up to around $\Psi = 22°$ which corresponds to $x/c \approx 2.7$ behind the trailing edge. In order to smooth the transition to the unstructured area there is a helical tube with tetrahedral cells around the block which have the same edge length as the hexahedral cells. The tube is positioned where the blade-tip vortex is expected. If not otherwise stated, the simulations were run with a vortical correction like Brandsma et al. [26]. This correction reduces the viscosity and therefore delays dissipation [27]. The top view in Fig. 3b shows a slice through the $c/4$-line and Fig. 3c the surface grid at the blade tip. A test

case which causes dynamic stall was investigated, with sinusoidal pitching at $\Theta_{root} = 23.0^\circ \pm 6^\circ$.

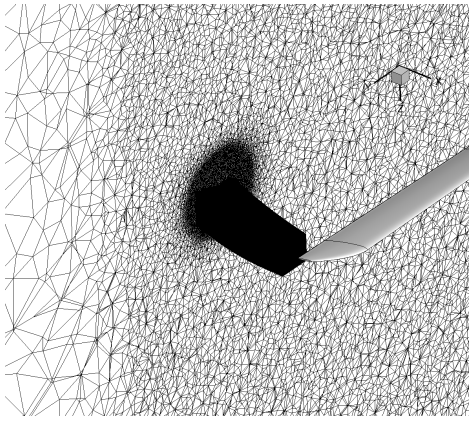

(a) Isometric view

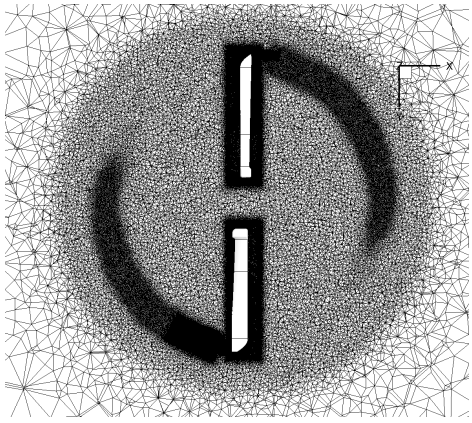

(b) Top view

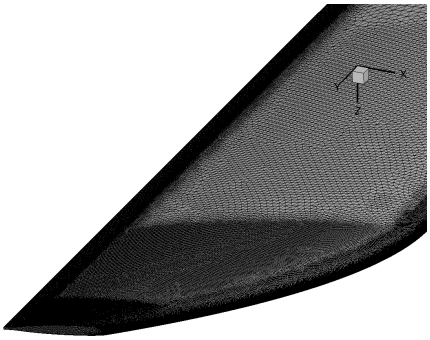

(c) Surface grid

Figure 3: Numerical grid.

4. COORDINATE SYSTEMS

The two coordinate systems which are used in this study are shown in Fig. 4.

Some results are expressed in planes captured by the PIV system. They correspond to planes which cut the rotor hub on the $c/4$ line and are rotated around the rotor axis by the wake age as depicted in Fig. 2. The origin of this coordinate system with the subscript p is on the circle which

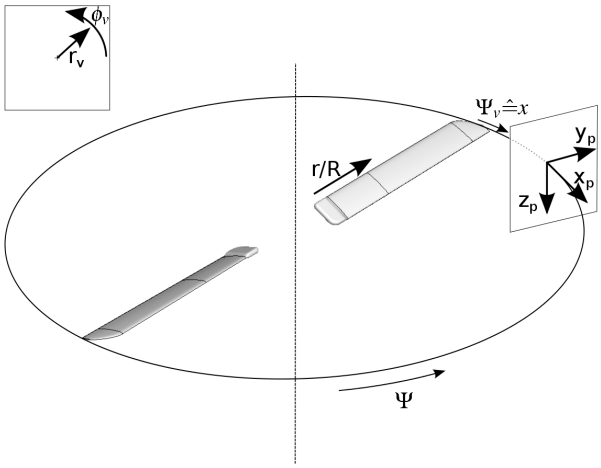

Figure 4: Coordinate systems employed in this study.

Table 2: Conversion of vortex age.

Ψ_V in $^\circ$	x/c
0.0	-0.73
4.64	0.0
7.3	0.41
10.0	0.84
20.0	2.42

is described by the rotation of the blade tip. The planes follow the rotor blade and are described by their curved distance x/c or Ψ_V behind the rotor blade. This coordinate system consists of a x_p-, y_p- and z_p-axes. The x_p-axis points away from the blade. The vorticity of the blade-tip vortex is positive in this coordinate system. The y_p-coordinate points outboard. A vortex movement towards the root results therefore in negative y_p-values. The z_p-axis complements the right-hand system and points accordingly downwards.

The two-dimensional vortex coordinate system is a translated and transformed polar description of the y_p and z_p plane of the p-coordinate system. It has its origin at the vortex core and is marked with the subscript v. The radial axis r_v is pointing outwards. The azimuthal axis ϕ_v is mathematically positive defined and starts on the right hand side when looking towards younger wake ages. Therefore a value of $\phi_v = 0^\circ$ corresponds to the y_p-axis.

Table 2 shows a conversion chart of the wake age which are defined in two ways. The first column states the azimuthal distance in degree between the considered measurement plane and the $c/4$ line of the vortex generating blade. The second column is the curved distance x up to the trailing edge normalized by the chord length c.

5. VORTEX ANALYSIS

Several vortex models exist in literature. A broad range is covered by an algebraic model of Vatistas et al. [28], which fits other models by tuning the parameter n. Ramasamy & Leishman [29] have created a new parametric mathematical formulation to cover an extensive scope of vortex Reynolds-numbers with up to six fit coefficients. Vortices can furthermore be divided into a wake-like or jet-like appearance depending on the axial velocity of the vortex. A wake-like vortex is defined as a vortex with an axial core velocity lower than the surrounding velocity U_∞ leading to a velocity deficit, whereas a vortex with an axial core velocity higher than U_∞ defines a jet-like behavior. For rotating blades with negligible inflow as investigated here, the definitions are transformed to the p-coordinate system. If the axial velocity u_p is positive, a jet-like behavior is derived, as the flow pushes in the opposite direction of the blade. A wake-like behavior exists if the axial velocity u_p is negative since the blade accelerates the flow in the blades direction of movement.

The experimental data is derived by planes in the three-dimensional field with in-plane and out-of-plane velocity components according to Fig. 2. The data evaluation of the PIV planes is described by Braukmann et al. [22]. To ensure a valid comparison between the numerical and experimental data two-dimensional cuts across the tip vortex in the computational fluid dynamics (CFD) simulations were extracted. The density was fitted to the density distribution (see Bagai & Leishman [30]) of the vortex model ($n = 2$) of Vatistas et al. [28] to define the position of the vortex core. The fitting of the vortex model allows a new sub-grid accuracy for the vortex position. The numerical results were then interpolated onto a cartesian grid around the estimated vortex core in the wake plane. Once the position has been defined, all investigated parameters like swirl velocity distribution, radius, circulation and the shape of the vortex core can be extracted.

The swirl velocity can be obtained with several procedures. The simplest method which is employed in the analysis of the experimental data is a binning of the already existing grids into annuli of equal thickness. All points which fall into one circular bin are combined to a mean swirl velocity leading to a distribution over a radial coordinate. Due to noncircular vortices this method can smear out aerodynamic effects. A better solution which is feasible for CFD data is to define radial cuts through the vortex core. To plot a swirl velocity distribution the values are gained by averaging the cuts. Additionally, the standard deviation can be shown indicating a noncircular shape of the vortex core. The circulation (Eq. 1) is proportional to the product of the swirl velocity v_ϕ and the radius r since it is the line integral around a closed curve of the velocity field. If the mean of a radial bin has already been extracted then the distribution of the circulation can be derived by multiplying the swirl velocity with the corresponding radius.

$$\Gamma = \oint v ds = 2\pi \cdot \Sigma v_{\phi_i} \cdot r \tag{1}$$

The radius of the vortex core is defined as the radial position with the highest swirl velocity. The vortex core radius is investigated for every radial cut through the vortex core and then combined to one value instead of averaging the cuts directly which would basically be the same method as the previous described binning. Ramasamy et al. [31] noted that two orthogonal cuts are sufficient to determine a mean value of the radius if the core seems elliptical, however since 90 radial cuts are used to determine the shape of the vortex they are also taken to determine the radius.

6. RESULTS AND DISCUSSION

6.1. Grid and time step sensitivity

A grid and time step sensitivity study was carried out numerically. The grid study focused on the behavior of the tip vortex by comparing the experimental data with three simulations of different numerical grids. Table 3 lists the edge length of the refined area and the number of nodes of the investigated background grids. One complete unstructured background grid and two grids with a refined block consisting of fine hexahedral cells were compared, focusing on the length of the cells in the blade-tip region.

Figure 5 shows the velocity distribution for attached flow during the upstroke motion for the experiment and simulations with different grid attributes of the background grid listed in Tab. 3. The peak swirl velocity in the experiment is found at $v_\phi/U_{\text{tip}} \approx 0.77$ at a nondimensional radial distance just below $r/c = 0.07$ which corresponds to approximately 5 mm. Both solutions with a structured hexahedral block predict a slightly larger radius with $r/c = 0.075$, with varying peak swirl velocities. The fine grid yields the highest swirl velocities and matches the experiment data best. Both "base" grids underestimate the swirl velocity with the same vortex core radius as the fine grid. The unstructured grid yields almost the same swirl velocity even though it has with $6.4 \cdot 10^6$ more nodes than the structured grid with $4.4 \cdot 10^6$ nodes. All simulations match each other outside the vortex core. Although the difference between the simulations at this young wake age are small, all further investigations were performed with the finest grid to assure similar agreement at older wake ages.

Table 3: Parameters of the background grid.

	$\Delta s/c \cdot 10^2$	node no. (million)
CFD unstruct. base	0.69	6.4
CFD struct. base	0.69	4.4
CFD struct. fine	0.34	13.4

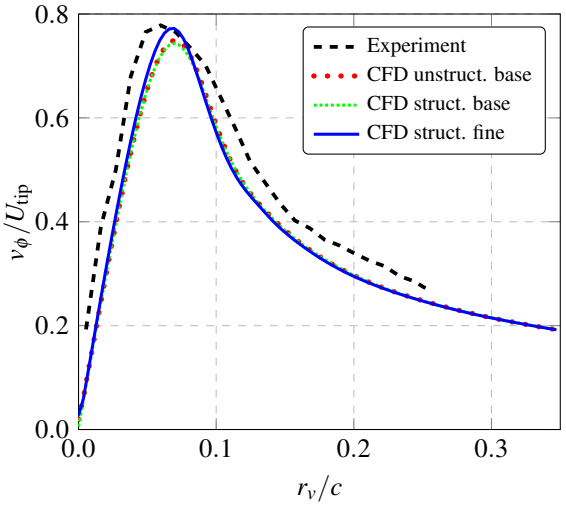

Figure 5: Swirl velocity of the blade-tip vortex at $\Psi_V = 7.3°$ ($x/c = 0.39$) behind the blade for different grids.

Figure 6 shows a study of the time discretization. There are still changes in the thrust coefficient after increasing the timesteps from 360 ($\Delta\Psi = 1.00°$) up to 1440 ($\Delta\Psi = 0.25°$). Kaufmann et al. [32] used up to 3000 time steps for their pitching period whereas Letzgus et al. [33] concluded a time step study on their rotating blade resulting in 1440 timesteps. The solutions with 200 or 400 inner iterations predict both the overshoot at the highest angle of incidence and match sufficiently each other during the upstroke. The time step of $\Delta\Psi = 0.25°$ (1440 time steps per period) with 400 inner iterations is therefore used for all following computations.

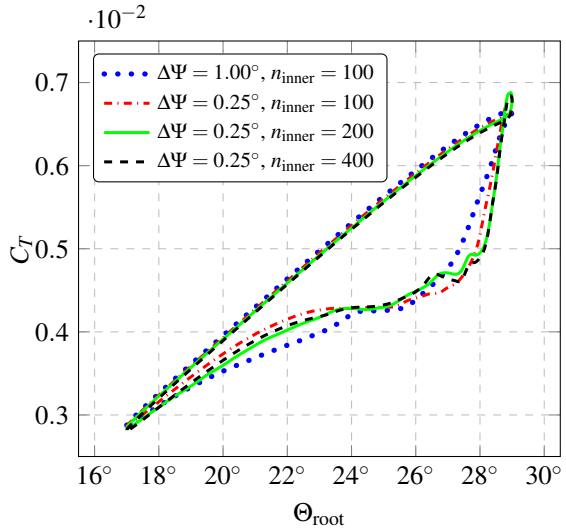

Figure 6: Thrust coefficient with different temporal resolution.

6.2. Comparison with the experiment

Figure 7 shows both the local lift and moment coefficients integrated from pressure sensors at $r/R = 0.77$ over a full period. The CFD data has additionally been integrated

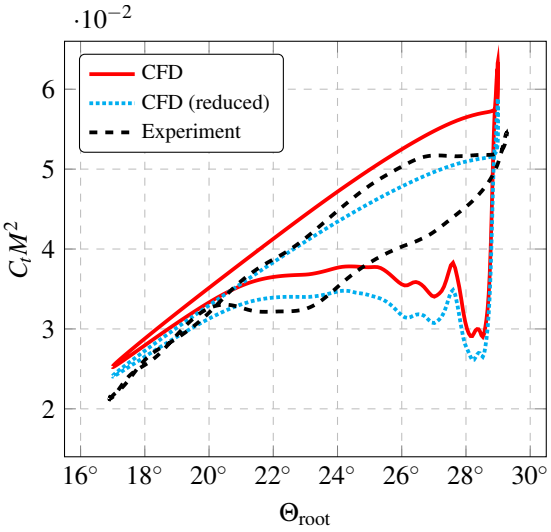

(a) Lift coefficient

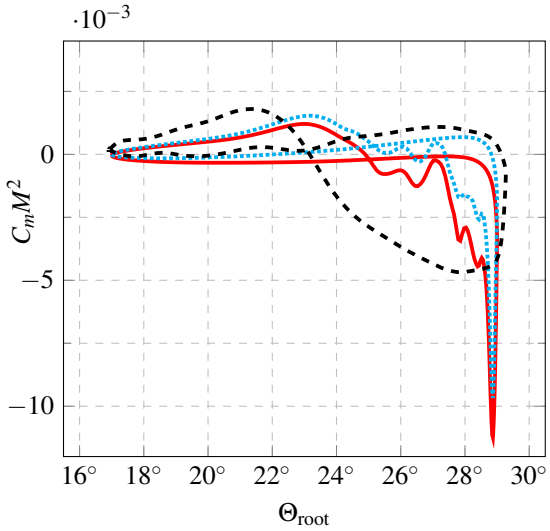

(b) Pitch moment coefficient

Figure 7: Dimensionless coefficients at $r/R = 0.77$.

with reduced points corresponding to the experimental sensor positions. Particularly at the lowest angle of attack, the effect of the free boundary layer transition in the experiment leads to differences in the lift compared with the fully turbulent CFD. In the CFD results there is a sudden drop at the highest angle of attack which results in a sharp moment coefficient minimum. The numerical simulation overpredicts the lift hysteresis which leads to an overprediction of the moment coefficient minimum, since the separation in the experiment is less pronounced. Nevertheless, the behavior between the experiment and CFD simulation is similar, and should be sufficient to compare the blade-tip vortices during the upstroke.

6.3. General aspects of blade-tip vortices

Figure 8 shows instantaneous isosurfaces of the λ_2-criterion [34] which are colored with the vorticity perpendicular to the wake plane at three different stages during

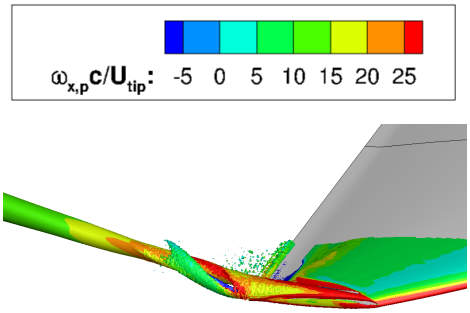

(a) $\Theta_{root,\,min} = 17.0°$

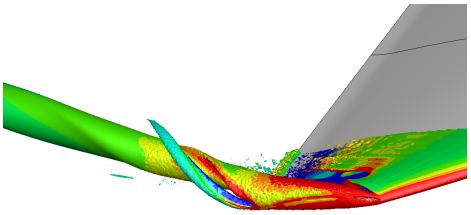

(b) $\Theta_{root} = 23.0° \uparrow$

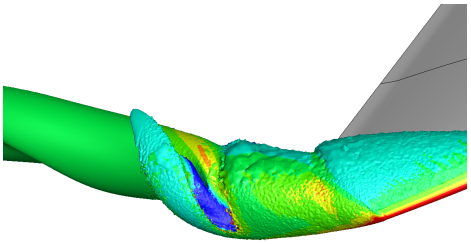

(c) $\Theta_{root,\,max} = 29.0°$

Figure 8: Isosurfaces of λ_2 criterion, colored with rotationwise vorticity.

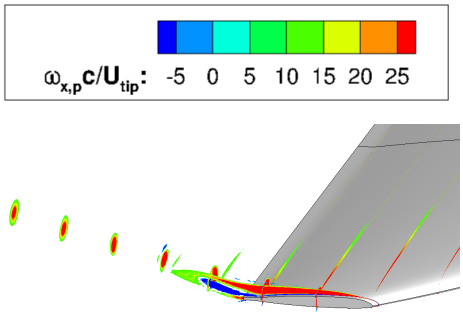

(a) $\Theta_{root,\,min} = 17.0°$

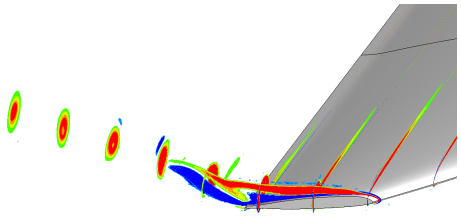

(b) $\Theta_{root} = 23.0° \uparrow$

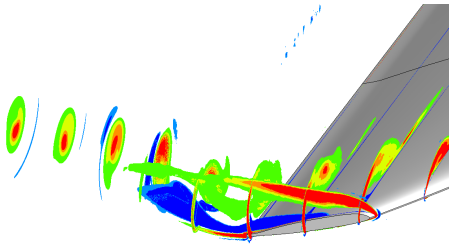

(c) $\Theta_{root,\,max} = 29.0°$

Figure 9: Slices at the blade tip, colored with rotationwise vorticity.

the upstroke motion. Red and green colors represent positive vorticity values and thus the expected rotation of the blade-tip vortex due to the pressure difference between the upper and lower surface. Blue colors indicate a counter-rotating vortex with negative vorticity values. Overall the size of the blade-tip vortex increases with increasing angle of incidence. At the highest angle of incidence (see Fig. 8c) the blade-tip vortex moves inboard of the blade tip, as also seen by Kaufmann et al. [16] for a nonrotating case.

Figure 9 highlights the formation of both rotational motions by showing vorticity colored slices. At the lowest angle of incidence (see Fig. 9a) a domain of negative vorticity values extends from the position of the trailing edge. This area is then entrained by the primary vortex and a positive global rotation is imposed on it. At higher angles of incidence (see Fig. 9b and Fig. 9c) negative vorticity already occurs on the upper surface of the blade. The primary blade-tip vortex evolves at the blade tip and lands on the upper surface further inboard than at a lower angle of incidence. The blade-tip vortex indicated by red and green colors does not follow the blade surface. Instead it is driven by the horizontal inflow and therefore separates from the blade-tip surface right after the leading edge.

6.4. Circulation

The circulation is derived as described in Sec. 5. The amount of circulation correlates to the lift generated since parts of the produced lift merge into the growing blade-tip vortex according to the theorems by Helmholtz and Kutta-Zhukovsky. The distribution of the circulation of a blade-tip vortex starts at zero in the core and after a short and rapid increase it approaches the total circulation asymptotically. Wolf et al. [15] identified $r_v = 0.2c$ as a suitable value of a constant radial distance for the evaluation of the circulation. This circulation $\Gamma_{0.2c}$ is a good substitute for the total circulation. The CFD data shows that the circulation is still increasing at that border, but to compare with the experimental data, which is limited by the PIV region, this constant radial distance is chosen for the evaluation of the circulation.

Figure 10 shows the circulation of the blade-tip vortex at

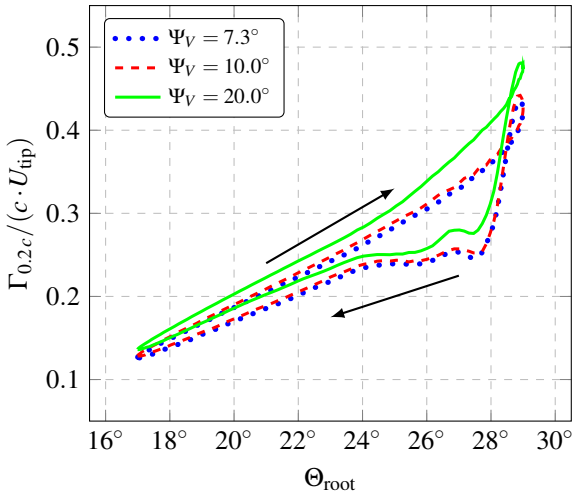

Figure 10: Circulation at constant radial distance $r_v = 0.2\,c$ for different wake ages.

a constant radial position $r_v = 0.2\,c$ away from the vortex core over the angle of incidence of the root at the formation time of the vortex. The circulation is normalized by the chord length c and the blade-tip velocity U_{tip}. It is noticeable that during the upstroke the gradient is fairly constant up to $\Theta_{\text{root}} \approx 24°$. At larger angles of incidence the circulation does not increase linearly anymore. The highest gradient is reached by the oldest wake age shown ($\Psi_V = 20.0°$). The shape of these graphs is of a similar shape to the lift coefficient in Fig. 7, but with lower hysteresis. Around the highest angle of incidence the circulation still increases during the downstroke motion until a sudden drop appears. The circulation is higher at older wake ages since parts of the blades wake-vorticity is entrained.

Figure 11 shows a comparison of the blade-tip vortex circulation and the lift coefficient at $r/R = 0.77$ by plotting the ratio Q (Eq. 2) of both values scaled by the ratio $Q_{\Theta_{\text{min}}}$ at $t/T = 0$.

$$Q = \frac{\Gamma_{0.2c}}{C_l M^2} \cdot \frac{C_l M^2(\Theta_{\text{min}})}{\Gamma_{0.2c}(\Theta_{\text{min}})} \tag{2}$$

The x-axis shows again the angle of incidence at the formation of the vortex and not the angle of incidence at that time. The scaling sets the ratio $Q = 1$ at $t/T = 0$. Again up to half the upstroke ($\Theta_{\text{root}} \approx 24$) the ratio Q stays almost constant for all three wake ages. It should be noted, that due to different circulation values within the wake ages all three curves are separately scaled and the curves therefore only state the relation between the lift coefficient and the blade-tip vortex circulation. At angles of incidence larger than $\Theta_{\text{root}} \approx 24°$ the ratio slightly increases to values $Q > 1$. At the maximum angle the ratio exceeds $Q > 2$ meaning the ratio between the vortex circulation and lift is twice as high as the ratio at the minimum angle of incidence. This value eventually reduces and after reattachment returns to $Q \approx 1$. This was already observed by Wolf et al. [15] in the nonrotating version of this experiment with a pitching blade. The blade-tip vortex has a stabilizing effect on dynamic stall as it delays separation on the blade tip. The lift coefficient drops after the highest angle of incidence resulting in a decreasing denominator of Q and therefore an increasing Q. After the peak of Q the vortex circulation starts then to decrease which reduces the counter of Q and therefore Q as well.

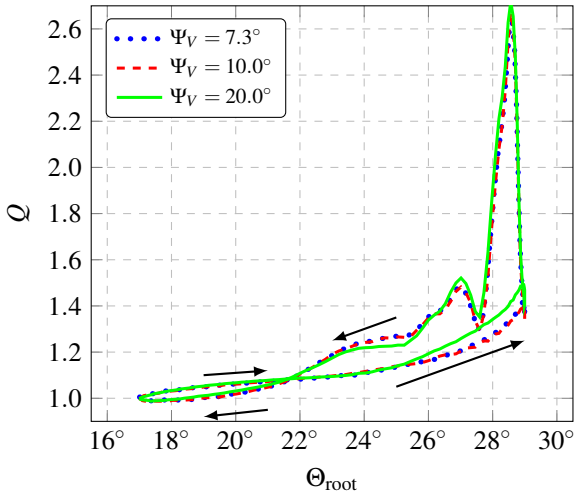

Figure 11: Comparison between tip vortex circulation and lift coefficient.

Figure 12 shows the circulation of the blade-tip vortex for the experiment and numerical simulation at the wake age $\Psi_V = 7.3°$. The two upper lines are derived by the line integral at the constant distance of $r_v = 0.2\,c$. The CFD simulation slightly underestimates the circulation measured in the experiment. Nevertheless, the overall trend is in good agreement, except for the dynamic stall region at $0.5 < t/T < 0.75$ where the numerical and experimental loads do not match well. One reason for the underestimation of $\Gamma_{0.2c}$ in the CFD data is the different vortex radius, since the CFD simulation predicts bigger radii at this wake age than the experiment. The constant radial distance is therefore relatively closer to the vortex core in the CFD data. For this reason, the two lower lines show the circulation integrated out to the edge of the vortex core. In that case the two lines agree very well with each other between $0.2 < t/T < 0.45$. In the domain $t/T < 0.2$ the two methods do not match anymore since the radius could not be predicted very well in the experiment due to a limit in the PIV resolution. Limitations of the PIV technique to measure helicopter blade-tip vortices are described by Raffel et al. [35] and references therein.

6.5. Radius

Figure 13 depicts the vortex radius for a full cycle at several planes behind the blade. The radius grows during the upstroke since more generated lift results in a stronger and larger vortex. A small hysteresis is existent since the radius is bigger during downstroke than during upstroke compared at the same angle of incidence. There is almost

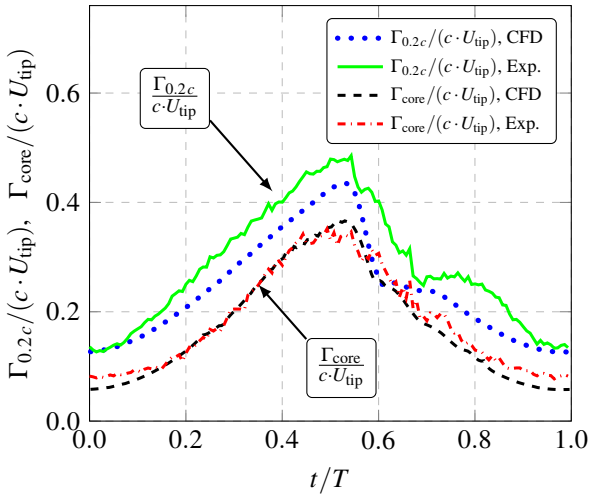

Figure 12: Circulation of the experiment [22] and CFD simulation at two different radial stations for $\Psi_V = 7.3°$.

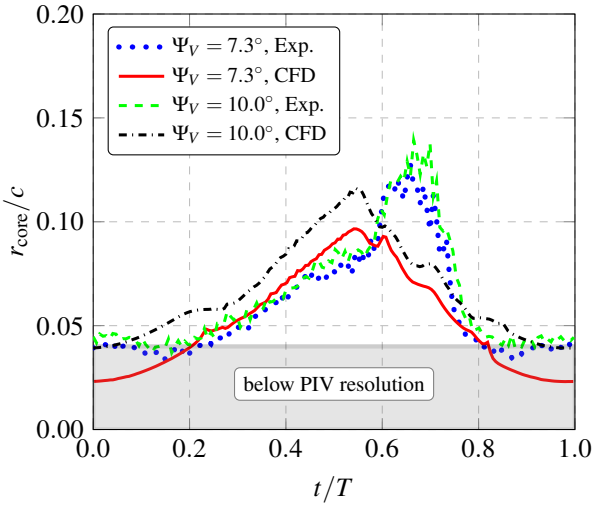

Figure 13: Vortex radius for experiment [22] and CFD at two different wake ages.

no increase in the experimental results of the vortex core radius identifiable between the wake ages $\Psi_V = 7.3°$ and $\Psi_V = 10.0°$ whereas due to numerical diffusion the radius of the vortex in the numerical data increases. With increasing vortex age, the results of the numerical simulation drift away from the experimental data. The numerical data at $\Psi_V = 7.3°$ matches the experimental radius in the upstroke motion up to $t/T \approx 0.5$ well, but during dynamic stall the results diverge. The experiment shows a sudden increase in the radius whereas the numerical data shows a smooth decrease. Braukmann et al. [22] however state that during the stall conditions high fluctuations and low swirl velocities lead to difficulties in detecting the radius in the experimental data. After reattachment, the two methods approach each other again. The radius in the CFD data underpredicts the experimental data around the lowest angle of incidence ($t/T < 0.2$ and $0.8 < t/T$). In this area, the CFD simulation states the radius to be $r_{\text{core}}/c < 0.05$. This is below the spatial PIV resolution and therefore the limit of the experimental detection of the vortex core. Structures smaller than the window size can not be correctly resolved by PIV.

6.6. Azimuthal analysis of the vortex core

The radial cuts through the vortex core are used to identify the shape of the vortex core by analyzing every cut on its own.

Figure 14 shows the shape of the vortex core obtained with 90 cuts through the vortex core center. The radius is detected at the maximum of the swirl velocity in the respective cut. Ramasamy et al. [31] stated that approximately 60 cuts are suitable to receive a valid result of the shape. Several shapes at constant wake age but at different time steps in the period are shown. It is clearly visible that during the upstroke motion the vortex core size increases. Due to the increasing angle of incidence there is more lift generated and therefore a higher pressure difference at the blade tip occurs. The shape of the vortex at $t/T = 0.23$ is not elliptical anymore, as a bulge at $\phi_v = 30°$ is formed. With increasing time this bulge is not always as clearly visible. Figure 15 shows the azimuthal variation of the swirl velocity on the vortex core. This peak swirl velocity is during the upstroke motion at $\phi_v \approx 315°$ only between $0.5 < v_\phi/U_{\text{tip}} < 0.6$. At $\phi_v \approx 135°$ the peak swirl velocities cover a wider range ($0.4 < v_\phi/U_{\text{tip}} < 0.7$). From both figures it can be concluded that both the radius and the maximum swirl velocity increase with increasing angle of incidence.

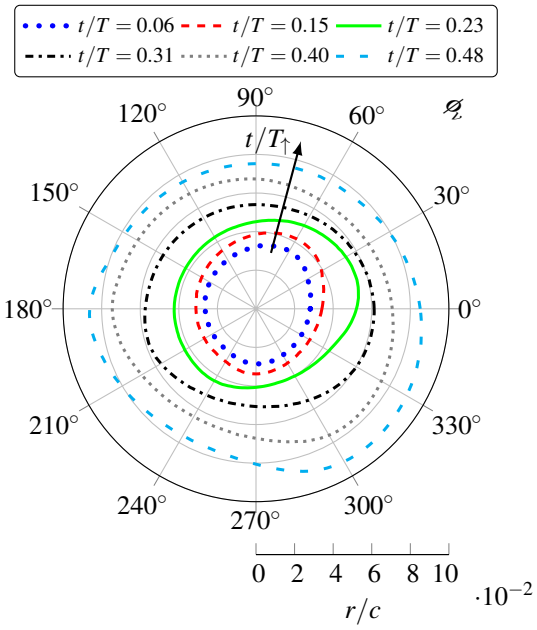

Figure 14: Vortex core shape for several time instants during upstroke at $\Psi_V = 7.3°$.

Figure 16 shows the parameters b/a and ϕ_v of the ellipse which has been fitted to the shape of the vortex core. Two parameters define the shape of an ellipse in

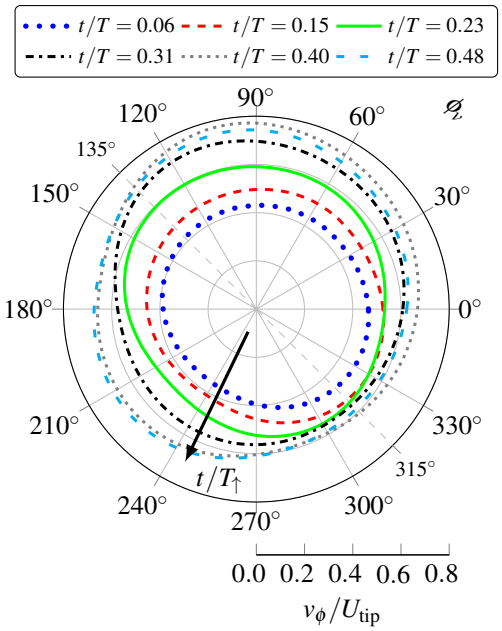

Figure 15: Peak swirl velocity on the vortex core for several time instants during upstroke at $\Psi_V = 7.3°$.

a two-dimensional plane. The two axes are divided into the major axis a and the minor axis b. Figure 16a shows the ratio b/a of the two axes over the reduced time for three different wake ages. The smaller the ratio, the more elliptical is the vortex core. At a vortex age of $\Psi_V = 10.0°$ the shape is at the instants of time with low angles of incidence $t/T < 0.2$ and $t/T > 0.8$ nearly a circle with a ratio of $b/a \approx 0.98$. A vortex two degrees younger ($\Psi_V = 8.0°$) shows still an elliptical shape with a ratio of $b/a \approx 0.9$. In all three wake ages the shape becomes more elliptical with increasing angle of incidence. Values in the middle ($0.2 < t/T < 0.8$) show a high scatter since not all shapes can be fitted by an ellipse. The second parameter is the inclination ϕ_v of the major axis to the y_p-axis, which is shown in Fig. 16b. A value of $\phi_v = 0°$ or $\phi_v = 180°$ means that the ellipse is stretched along the y_p-axis. A positive value stands for an ellipse which is tilted towards the mathematically positive direction. A fully upright ellipse (along z_p-axis) is denoted by a value of $\phi_v = 90°$ or $\phi_v = -90°$ respectively. Values in the middle ($0.2 < t/T < 0.8$) have to be taken with care since the vortex core shape can not satisfactorily fitted to an ellipse anymore. A rotation is already detectable between the three different wake ages. The youngest vortex at $\Psi_V = 7.3°$ is almost fully upright at the smallest angle of incidence with an inclination of $\phi_v \approx 90°$. Only $\Delta\Psi_V = 0.7°$ later the vortex core has turned more than $\Delta\phi_v = 45°$ in anti-clockwise direction and has an inclination of $\phi_v \approx 145°$. Two degrees older, the vortex is again, after turning anti-clockwise, in an almost upright position. In that short distance the shape of the vortex has therefore rotated a half anti-clockwise rotation which is in the sense of rotation of the tip vortex. With increasing angle of incidence, the inclination first rises and then drops down doing a clockwise rotation. In the end of the downstroke, the vortex does an anti-clockwise rotation.

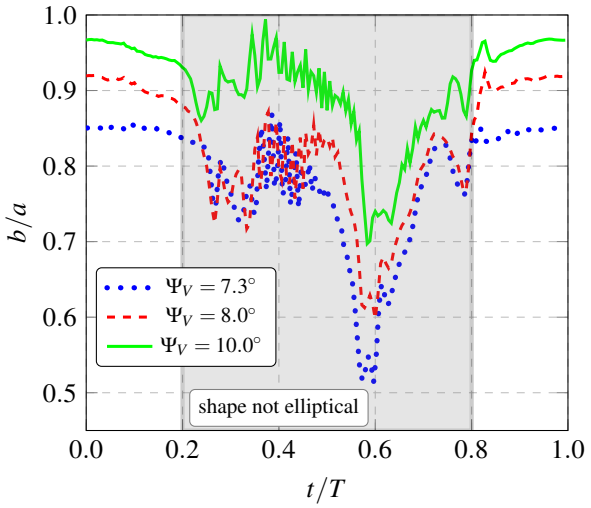

(a) Ratio b/a of the minor axis to the major axis of the ellipse

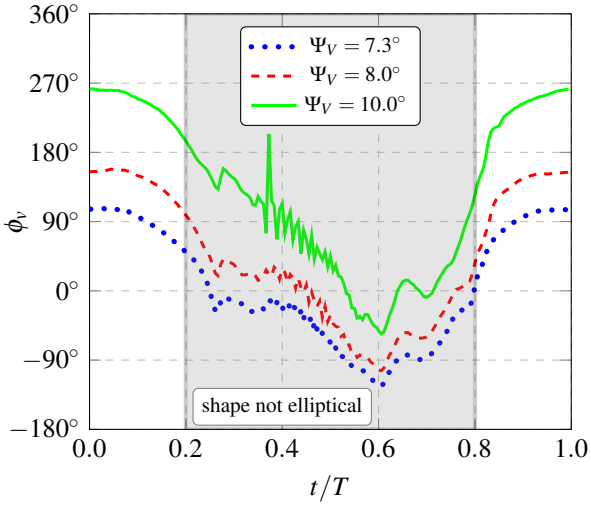

(b) Inclination i of the ellipse

Figure 16: Parameters of the ellipse fitted to the vortex core.

6.7. Position

Figure 17a shows the vortex position at different wake ages behind the blade throughout a full cycle. The position is extracted with the methods described in Sec. 5. The position at the lowest angle of incidence is always in the top right corner. At this point, the generated lift is the lowest, leading to the smallest inboard drive. The strong vertical movement is imposed by the prescribed vertical movement of the trailing edge due to the pitching motion. Halfway through the upstroke, the motion starts to get chaotic with an anti-clockwise rotation of the shape setting in. A vertical correction, which shows the vortex-core position with respect to the trailing edge is shown in Fig.17b exhibiting a stronger horizontal than

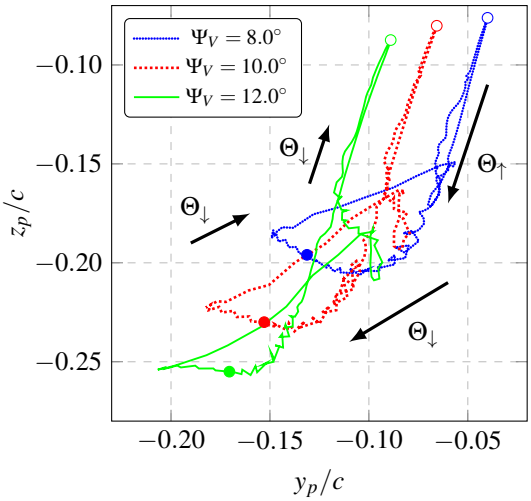

(a) Position of the vortex core with respect to the p-coordinate system (related to the $c/4$ position of the blade)

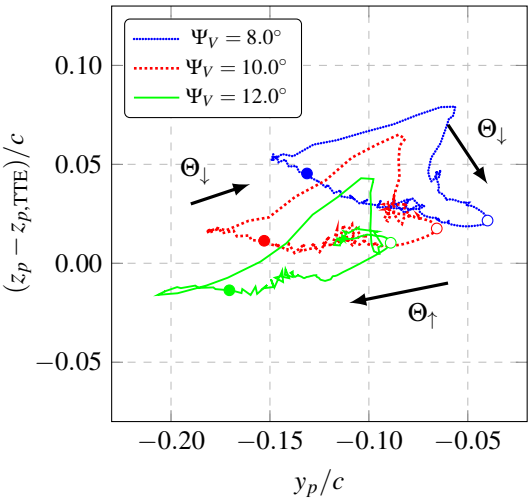

(b) Position of the vortex core with respect to the blade tip trailing edge (TTE)

Figure 17: Position of the vortex core throughout a full cycle, the highest angle of incidence is represented with colored circles, and white filled circles represent the lowest angle of incidence respectively.

vertical motion of the vortex core. The highest position $(z_p - z_{p,\mathrm{TTE}})/c$ is detected during the downstroke motion. For young vortices up to $\Psi_V = 10.0°$, the vortex always stays above the trailing edge. The timewise motion of the vortex can be drawn by comparing the different graphs yielding a consistent downwards and inboard movement. During the upstroke motion, an orbital pattern is revealed in both figures, which occurs at the same time instant when the axial pressure gradient inside the vortex core reaches a maximum and the vortex breaks down. This leads to an asymmetrical appearance of the vortex. At further increasing angles of incidence, the circle-like vortex core vanishes; the area with the highest negative value of λ_2 is shifted towards one side and a spiral movement sets in leading to a primary shift inboard superimposed with a rotation of the vortex core itself.

Figure 18 shows the tip vortex visualized by the λ_2 criterion for several wake ages and time instants. All plots in a horizontal row are extracted at the same time instant. A value of $t/T = 0$ means that the blade is at its lowest angle of incidence. All plots show situations during the upstroke motion. The upper row shows the earliest situation. Each following row shows the situation $\Delta t/T = 2/360 \approx 5.5 \cdot 10^{-3}$ later, which implies the movement of the blade in that time frame to be exactly $\Delta\Psi = 2°$. Every row shows furthermore three different planes which correspond to increasing wake age in steps of $\Delta\Psi_V = 2°$. Every plot in one vertical column is extracted at the same wake age. This leads to the ability to follow slices of the vortex in time. The vortex in the upper left plot is $\Delta t/T = 2/360$ later, exactly $\Delta\Psi_V = 2°$ older and therefore depicted in the picture diagonal south east. The black arrows show the evolution of one vortex in time. This applies to all other pictures too. All columns correspond to a plane following the blade under a defined angle. Most data in this study is displayed in this way. In the left column it can be seen, that the area with the highest negative λ_2 value (blue color) is not circularly distributed. This area which matches the lowest density has a spin inside the vortex leading to an orbital movement of the vortex core. This is not just a rotation within the period (column-wise perspective) since it is also visible row-wise. A row corresponds to a frozen situation which is a single solution of the numerical simulation. In the first row the blue area starts in the upper right area and $\Delta\Psi_V = 2°$ later the blue area faces downward. The spin is strongest when following the evolution of a vortex on its fixed geodesic position (indicated by the arrows). The vortices have a spin with offsets dependent on the age which leads to a timewise spin and a spin along a vortex tube. Gursul et al. [36] describe the vortex breakdown as a dramatic flow disruption accompanied with a spiral winding in an opposite sense of rotation of the vortex.

6.8. Pressure inside vortex core

All examined vortex cores yield a wake-like appearance which is forced by a positive pressure gradient along the vortex tube. Figure 19 shows the pressure along the axes of the vortex for a complete period. The pressure inside a vortex is, due to centrifugal forces, lowest on the core axis. The stronger the vortex is the lower the pressure is. The arrow ① indicates the progress at the lowest angle of incidence pointing towards older wake ages. The pressure increases with increasing vortex age to an asymptotic value which conforms to the surrounding conditions once the vortex disappears. Due to the pitching motion a second effect is superimposed onto this behavior. During the upstroke motion the vortex becomes stronger leading to a timewise decreasing pressure inside the vortex. The arrow

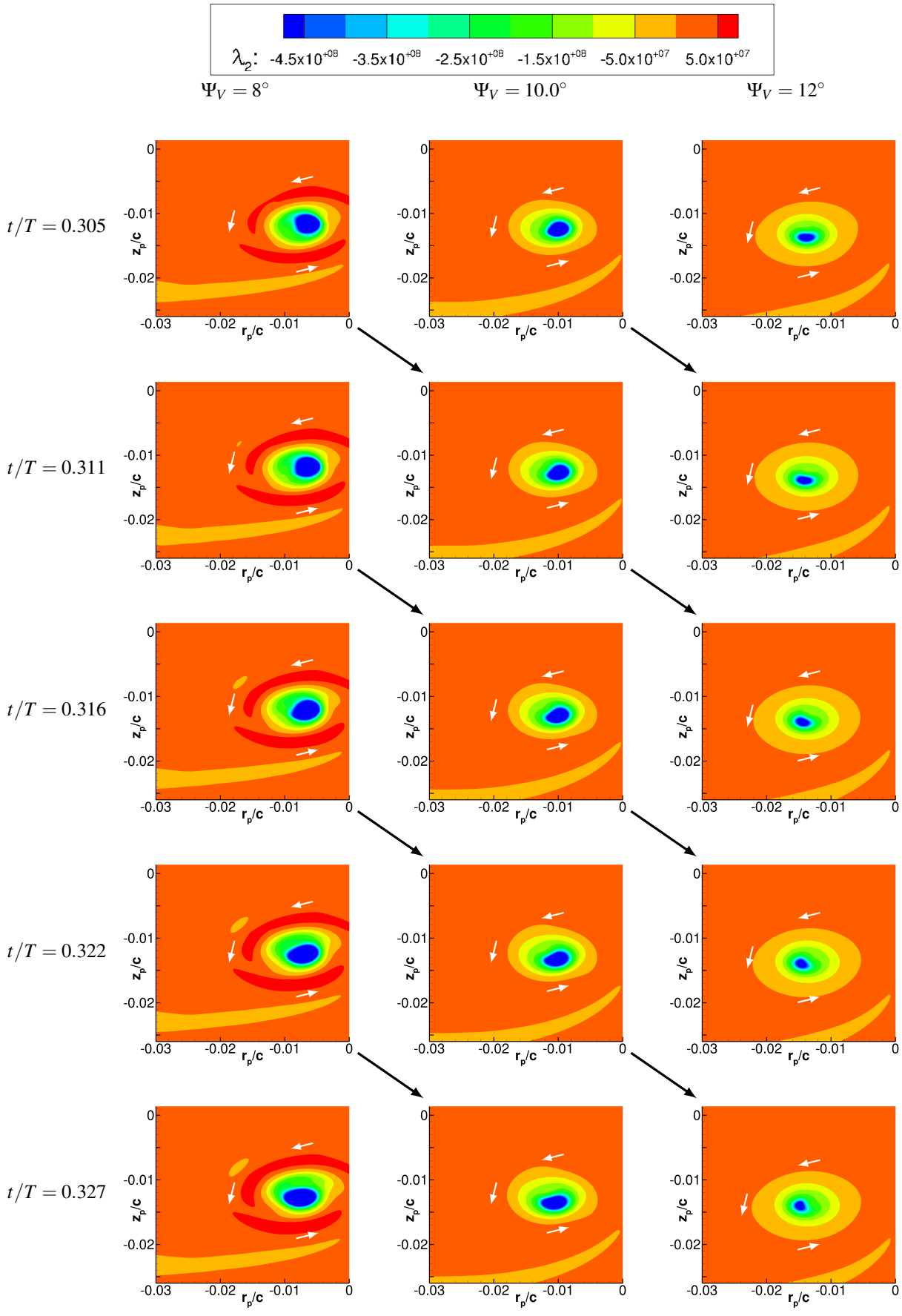

Figure 18: Vortex behavior at different wake ages and time instants during upstroke motion visualized by λ_2 criterion, black arrows show the evolution of one vortex, white unscaled arrows depict the sense of streamlines.

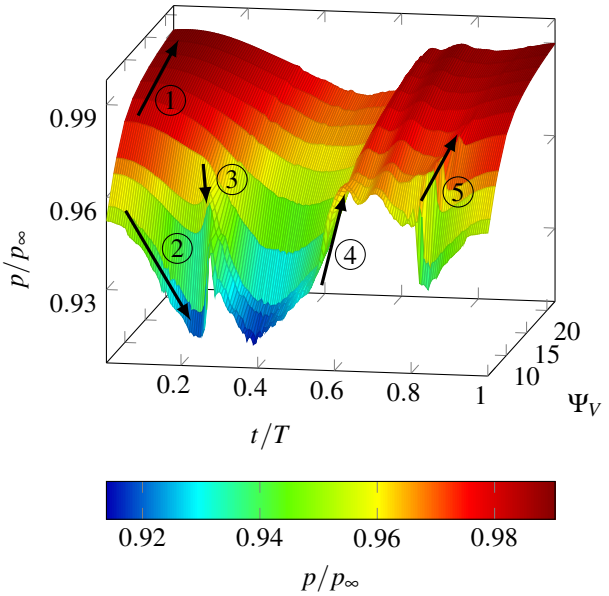

Figure 19: Pressure along vortex tube over the period.

② highlights this effect at a constant young wake age. Both effects work in the same direction, thus the overall gradient along a vortex core, which is similar to a total differential, increases. Halfway through the upstroke there is a wave-like appearance of a local pressure maximum visible which moves towards the blade, indicated by ③. First this hump occurs at $\Psi_V = 8°$ and $t/T \approx 0.25$, which is a sign of vortex breakdown, as Visbal [37] states that the pressure gradient along the vortex axis has a major influence on the initiation of vortex breakdown above a pitching delta wing. Garmann & Visbal [38] observed vortex breakdown with abrupt flow reversal on revolving wings to be driven by the pressure gradient and not by local Reynolds number. Around $t/T = 0.4$ the pressure reaches its minimum visible in Fig. 19. The flow separates at $t/T \approx 0.55$ which corresponds to the arrow ④ in Fig. 19, when the pressure at young wake ages rises towards the situation that the pressure is almost constant inside the vortex tube. The arrow ⑤ marks a drop in the pressure which coincides with the reattachment process. This drop moves downstream like a wave.

For clarity three distributions of different wake ages are plotted in Fig. 20. They are extracted from the same data as shown in Fig. 19. Additionally, the pressure distribution at $\Psi_V = 8°$ of a simulation without vortical correction is shown. The arrows are transferred with the same number. At $t/T \approx 0.2$ there is still a difference between the pressure at $\Psi_V = 8°$ and $\Psi_V = 10.0°$. This difference diminishes with increasing time by reduction in the pressure at $\Psi_V = 10$ and an increase at $\Psi_V = 8°$. This timewise maximum moves towards younger wake ages. The pressure at $t/T \approx 0.4$ is almost two percent higher if no vortical correction is implemented.

Figure 21 shows the effect of the vortical correction method by additionally showing the results at the wake age

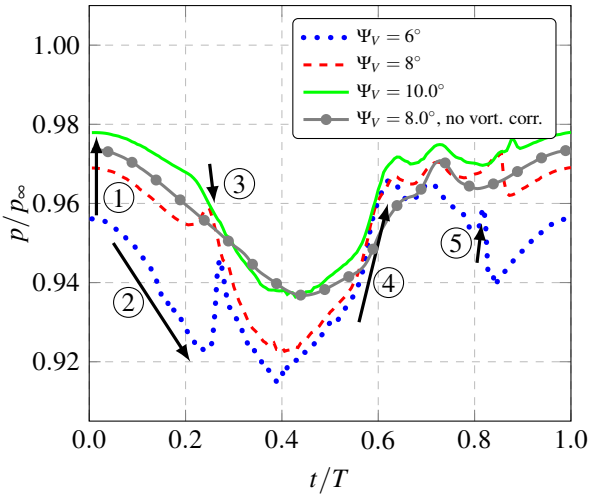

Figure 20: Pressure inside the vortex tube over a complete period at several constant wake ages.

of $\Psi_V = 8.0°$ of a simulation without vortical correction. At $t/T = 0.2$ the absolute value of u_p jumps to values higher than the blade tip velocity, which coincides with the reduced time when the vortex starts an orbital, rotational and meandering movement. The vortical correction reduces the viscosity in order to delay the numerical dissipation. The production term is varied using the ratio of the strain term to the vorticity term as sensor [27]. In this study the ratio is small due to the small free-stream velocity. The increase in the production term of vorticity leads to a decreased turbulent kinetic energy. It is known that without vortical correction the vortex diffuses too quickly since too much eddy viscosity is produced. The distinct peak at $t/T \approx 0.3$ is not detectable in both the core pressure and axial velocity in the simulations without vortical correction. The axial velocity is smooth and reaches up to 60% of the blade tip velocity.

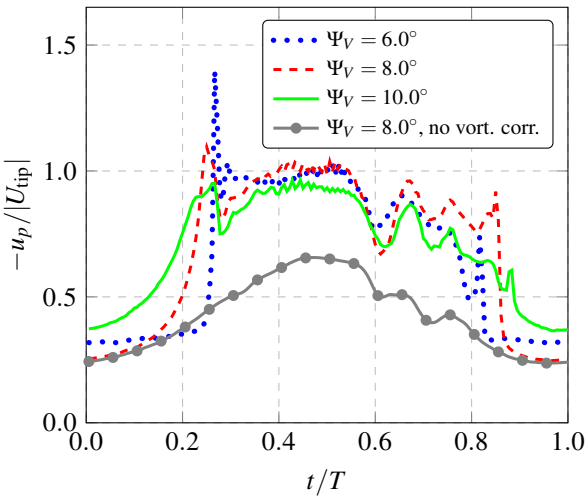

Figure 21: Axial velocity inside the vortex tube over a complete period at several constant wake ages.

7. EFFECT OF ROTATION

Kaufmann et al. [16] showed a comparison between their numerical investigations and experimental data of a pitching rotor blade tip model. The same airfoil DSA-9A is used along the span with a positive twist towards the blade tip, and the same SPP8 blade tip shape. The blade tip model has a chord length of 0.27 m and the pitching motion leads to dynamic stall on the model. Kaufmann et al. [16] implemented a higher temporal resolution with only half the resolution in the spatial domain. The background grid consisted purely of tetrahedral cells. Since their investigation was without rotation, the effect of rotation on the blade-tip vortex can be analyzed. The circulation is normalized using the flow velocity U_{70}, since the blade experiences in the rotational case a linearly increasing flow velocity.

Figure 22 shows the circulation in the blade-tip vortex at a constant radial distance of $r_v = 0.2c$ of this study and data taken of Kaufmann et al. [16]. The two experiments were analyzed at different wake ages. Therefore numerical data of this study is additionally shown at the equivalent wake age ($x/c = 0.25$) of the nonrotating investigation. The wake-age difference is negligible since there is almost no difference between the numerical data. During the upstroke motion ($0 < t/T < 0.5$), the nonrotational results match well. The level of the normalized circulation is in the same order for both cases.

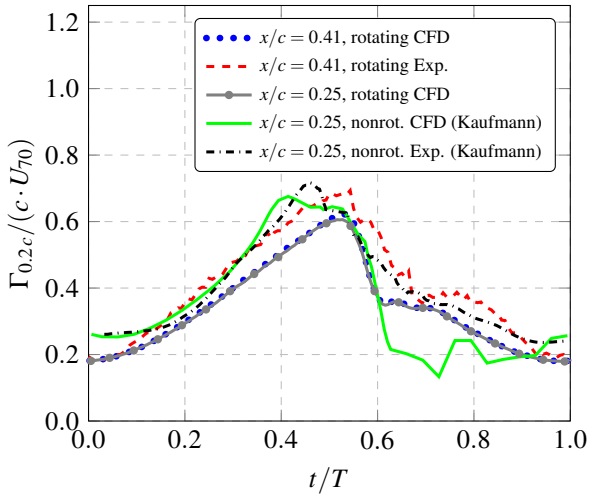

Figure 22: Circulation for experiment and CFD, nonrotational data after Kaufmann et al. [16], $\Psi_V = 7.3°$ ($x/c = 0.41$).

8. CONCLUSION

Unsteady RANS simulations of the blade-tip vortex of a two-bladed DSA9A-rotor have been compared to PIV measurements of the same setup. The investigations are carried out with a constant flow perpendicular to the rotor axes simulating a climb flight. The analysis demonstrates that the CFD simulations are capable in predicting the flow structures during tip-vortex generation and development in the near field of the blade. However, both, unstructured and structured grids, struggle with older vortices due to numerical dissipation.

The following findings have been drawn from this paper.

1. The vertical position of the vortex core is mainly driven by the position of the trailing edge. Any pitching motion dominates the position of the descending vortex.

2. Hexahedral cells conserve the vortical flow better than tetrahedral cells.

3. The wing tip vortex becomes stronger with increasing angle of attack even after stalled flow on the wing.

4. CFD is capable of matching the experimental results at young vortex ages $\Psi_V = 7.3°$ ($x/c = 0.41$). This includes the swirl velocity distribution, the circulation and the radius. At $\Psi_V = 10.0°$ ($x/c = 0.84$) some results are still valid whereas at $\Psi_V = 20.0°$ numerical diffusion is too large for matching results.

5. The vortex core exhibits an elliptical shape with an uncentered barycenter leading to an uneven rotation, if vortical correction is used. The vortical correction leads to high axial velocities and eventually to a vortex breakdown.

6. The more separated the flow is the less circular the vortex is.

7. The circulation of the blade-tip vortex is in the same order for a rotating and a nonrotating version of the used blade.

ACKNOWLEDGMENTS

The authors gratefully acknowledge the Gauss Centre for Supercomputing e.V. (GCS, www.gauss-centre.eu) for funding this project by providing computing time on the GCS supercomputer SuperMUC at Leibniz Supercomputing Centre (LRZ, www.lrz.de).

Funding of the DLR project FAST-Rescue is highly appreciated.

The authors would like to thank Christian Wolf and Kurt Kaufmann for the valuable discussions.

COPYRIGHT STATEMENT

REFERENCES

[1] F. Richez, "Numerical Analysis of Dynamic Stall for Different Helicopter Rotor Flight Conditions," *AHS 73rd Annual Forum*, Fort Worth, Texas, May 9–11, 2017.

[2] J. S. Chow, G. G. Zilliac, and P. Bradshaw, "Mean and Turbulence Measurements in the Near Field of a Wingtip Vortex," *AIAA Journal*, Vol. **35**, No. 10, 1997, pp. 1561–1567.

[3] W. J. Devenport, M. C. Rife, S. I. Liapis, and G. J. Follin, "The Structure and Development of a Wing-Tip Vortex," *Journal of Fluid Mechanics*, Vol. **312**, 1996, pp. 67–106.

[4] D. Birch, T. Lee, F. Mokhtarian, and F. Kafyeke, "Structure and Induced Drag of a Tip Vortex". *Journal of Aircraft*, Vol. **41**, No. 5, 2004, pp.1138–1145.

[5] P. B. Martin, J. G. Leishman, G. J. Pugliese, and S. L. Anderson, "Stereoscopic PIV Measurements in the Wake of a Hovering Rotor," *AHS 56th Annual Forum*, Virginia Beach, VA, May 2–4, 2000.

[6] K. W. McAlister, "Rotor Wake Development during the First Revolution," *AHS 59th Annual Forum*, Phoenix, Arizona, May 6–8, 2003.

[7] K. Duraisamy, M. Ramasamy, J. D. Baeder, and J. G. Leishman, "High-Resolution Computational and Experimental Study of Rotary-Wing Tip Vortex Formation," *AIAA Journal*, Vol. **45**, No. 11, 2007, pp. 2593–2602.

[8] J. Dacles-Mariani, G. G. Zilliac, J. S. Chow, and P. Bradshaw, "Numerical/Experimental Study of a Wingtip Vortex in the Near Field," *AIAA Journal*, Vol. **33**, No. 9, 1995, pp.1561–1568.

[9] K. Mohamed, S. Nadarajah, and M. Paraschivoiu, "Detached-Eddy Simulation of a Wing Tip Vortex at Dynamic Stall Conditions," *Journal of Aircraft*, Vol. **46**, No. 4, 2009, pp.1302–1313.

[10] J. E. W. Lombard, D. Moxey, and S. J. Sherwin, "Implicit Large-Eddy Simulation of a Wingtip Vortex," *AIAA Journal*, Vol. **54**, No. 2, 2016, pp. 506–518.

[11] D. J. Garmann and M. R. Visbal, "Unsteady Evolution of the Tip Vortex on a Stationary and Oscillating NACA0012 Wing," *54th AIAA Aerospace Sciences Meeting*, San Diego, California, January 4–8, 2016.

[12] D. J. Garmann and M. R. Visbal, "Further Investigations of the Tip Vortex on an Oscillating NACA0012 Wing," *46th AIAA Fluid Dynamics Conference*, Washington, D.C., June 13–17, 2016.

[13] D. J. Garmann and M. R. Visbal, "Investigation of the Unsteady Tip Vortex Structure on a NACA0012 Wing at Fixed Incidence," *55th AIAA Aerospace Sciences Meeting*, Grapevine, Texas, January, 9–13, 2017.

[14] Z. Lietzau, M. Ramasamy, R. Jain, J. G. Leishman, and J. Ekaterinas, "Comparison of Advanced RANS Modeling with Dual-Plane PIV Measurements for a Hovering Rotor," *AHS 73rd Annual Forum*, Fort Worth, Texas, May 9–11, 2017.

[15] C. C. Wolf, C. B. Merz, K. Richter, and M. Raffel, "Tip-Vortex Dynamics of a Pitching Rotor Blade-Tip Model," *AIAA Journal*, Vol. **54**, No. 10, 2016, pp. 2947-2960.

[16] K. Kaufmann, C. C. Wolf, C. B. Merz, and A. D. Gardner, "Numerical Investigation of Blade-Tip-Vortex Dynamics," *17th ONERA-DLR Aerospace Symposium*, Aussois, France, June 7–9, 2017.

[17] C. B. Merz, C. C Wolf, K. Richter, K. Kaufmann, A. Mielke, and M. Raffel, "Spanwise Differences in Static and Dynamic Stall on a Pitching Rotor Blade Tip Model," *Journal of the American Helicopter Society*, Vol. **62**, No. 1, 2017, pp. 1–11.

[18] K. Kaufmann, C.B. Merz, and A. D. Gardner, "Dynamic Stall Simulations on a Pitching Finite Wing," *Journal of Aircraft*, published online 2017.

[19] T. Schwermer, A. D. Gardner, and M. Raffel, "Dynamic Stall Experiments on a Rotor with High Cyclic Setting in Axial Inflow," *AHS 73rd Annual Forum*, Fort Worth, Texas, May 9–11, 2017.

[20] T. Schwermer, K. Richter, and M. Raffel, "Development of a Rotor Test Facility for the Investigation of Dynamic Stall," *New Results in Numerical and Experimental Fluid Mechanics X*, edited by A. Dillmann, G. Heller, E. Krämer, C. Wagner, and C. Breitsamter, Springer International Publishing Switzerland, 2016, pp. 663–673.

[21] J. Letzgus, A. D. Gardner, T. Schwermer, M. Keßler, and E. Krämer, "Investigation of Dynamic Stall on a Rotor with Cyclic Pitch Control," *43rd European Rotorcraft Forum*, Milan, Italy, September 12–15, 2017.

[22] J. N. Braukmann, T. Schwermer, and C. C. Wolf, "Investigation of Young Blade-Tip Vortices at a Rotor Test Facility using Stereoscopic PIV," *25. Fachtagung "Experimentelle Strömungsmechanik"*, Karlsruhe, Germany, September 5–7, 2017.

[23] D. Schwamborn, A. D. Gardner, H. von Geyr, A. Krumbein, H. Lüdeke, and A. Stürmer, "Development of the TAU-Code for Aerospace Applications," *50th International Conference on Aerospace Science and Technology*, Bangalore, India, June 26–28, 2008.

[24] F. R. Menter, "Zonal Two Equation k-ω Turbulence Models for Aerodynamic Flows," *24th AIAA Fluid Dynamics Conference*, Orlando, FL, July 6–9, 1993.

[25] S. Braun, A. Uhl, B. Eisfeld, and E. Stumpf, "Numerical Simulation of Vortex Roll-Up Processes Using the SSG/LRR-ω Model," *New Results in Numerical and Experimental Fluid Mechanics X*, edited by A. Dillmann, G. Heller, E. Krämer, C. Wagner, and C. Breitsamter, Springer International Publishing Switzerland, 2016, pp. 481–491.

[26] F. J. Brandsma, J. C. Kok, H. S. Dol, and A. Elsenaar, "Leading Edge Vortex Flow Computations and Comparison with DNW-HST Wind Tunnel Data," Technical report, NLR-TP-2001-239, 2001.

[27] K. Weinman, "Vortical Correction Modeling in the DLR TAU Code," *New Results in Numerical and Experimental Fluid Mechanics VIII*, edited by A. Dillmann, G. Heller, H. P. Kreplin, W. Nitsche, and I. Peltzer, Springer-Verlag Berlin Heidelberg, 2013, pp. 439–446.

[28] G. H. Vatistas, V. Kozel, and W. C. Mih, "A Simpler Model for Concentrated Vortices," *Experiments in Fluids*, Vol. **11**, No. 1, 1991, pp. 73–76.

[29] M. Ramasamy and J. G. Leishman, "A Reynolds Number-Based Blade Tip Vortex Model," *Journal of the American Helicopter Society*, Vol. **51**, No. 3, 2007, pp. 214–223.

[30] A. Bagai and J. G. Leishman, "Flow Visualization of Compressible Vortex Structures using Density Gradient Techniques," *Experiments in Fluids*, Vol. **15**, No. 6, 1993, pp. 431–442.

[31] M. Ramasamy, B. Johnson, T. Huismann, and J. G. Leishman, "Digital Particle Image Velocimetry Measurements of Tip Vortex Characteristics using an Improved Aperiodicity Correction," *Journal of the American Helicopter Society*, Vol. **54**, No. 1, 2009, pp. 1–13.

[32] K. Kaufmann, M. Costes, F. Richez, A. D. Gardner, and A. Le Pape, "Numerical Investigation of Three-Dimensional Dynamic Stall on an Oscillating Finite Wing," *Journal of the American Helicopter Society*, Vol. **60**, No. 3, 2015, pp. 1–12.

[33] J. Letzgus, M. Keßler, and E. Krämer, "CFD-Simulation of Three-Dimensional Dynamic Stall on a Rotor with Cyclic Pitch Control," *41st European Rotorcraft Forum*, Munich, Germany, September 1–4, 2015.

[34] J. Jeong and F. Hussain, "On the Identification of a Vortex," *Journal of Fluid Mechanics*, Vol. **285**, 1995, pp. 69–94.

[35] M. Raffel, A. Bauknecht, M. Ramasamy, G. K. Yamauchi, J. T. Heineck, and L. N. Jenkins, "Contributions of Particle Image Velocimetry to Helicopter Aerodynamics," *AIAA Journal*, published online 2017.

[36] I. Gursul, R. Gordnier, and M. Visbal, "Unsteady Aerodynamics of Nonslender Delta Wings," *Progress in Aerospace Sciences*, Vol. **41**, 2005, pp. 515–557.

[37] M. R. Visbal, "Onset of Vortex Breakdown above a Pitching Delta Wing," *AIAA Journal*, Vol. **32**, No. 8, 1994, pp. 1568–1575.

[38] D. J. Garmann and M. R. Visbal, "Dynamics of Revolving Wings for Various Aspect Ratios," *Journal of Fluid Mechanics*, Vol. **748**, 2014, pp. 932–956.